PAPER

Modeling of carbon pellets disruption mitigation in an NSTX-U plasma

To cite this article: C.F. Clauser *et al* 2021 *Nucl. Fusion* **61** 116003

IOP Publishing | International Atomic Energy Agency Nuclear Fusion

Nucl. Fusion **61** (2021) 116003 (11pp) https://doi.org/10.1088/1741-4326/ac233b

Modeling of carbon pellets disruption mitigation in an NSTX-U plasma

C.F. Clauser[1,2,*], S.C. Jardin[2], R. Raman[3], B.C. Lyons[4] and N.M. Ferraro[2]

[1] Lehigh University, Bethlehem, Pennsylvania 18015, United States of America
[2] Princeton Plasma Physics Laboratory, Princeton, New Jersey 08543, United States of America
[3] University of Washington, Seattle, Washington 98195, United States of America
[4] General Atomics, San Diego, California 92121, United States of America

E-mail: cclauser@lehigh.edu

Received 28 June 2021, revised 19 August 2021
Accepted for publication 2 September 2021
Published 4 October 2021

Abstract

Single carbon pellet disruption mitigation simulations using M3D $-$ C^1 were conducted for an NSTX-U-like plasma to support the electromagnetic pellet injection concept. A carbon ablation model has been implemented in M3D $-$ C^1 and tested with available data. 2D simulations were conducted in order to estimate the amount of carbon needed to quench the plasma, finding that the content in a 1 mm radius vitreous carbon pellet ($\sim 3.2 \times 10^{20}$ atoms) would be enough if it is entirely ablated. 3D simulations were performed, scanning over pellet velocity and parallel thermal conductivity, as well as different injection directions and pellet concepts (solid pellets and shell pellets). The sensitivity of the thermal quench and other related quantities to these parameters has been evaluated. A 1 mm radius solid pellet only partially ablates at velocities of 300 m s^{-1} or higher, thus being unable to fully quench the plasma. To further enhance the ablation, approximations to an array of pellets and the shell pellet concept were also explored. 3D field line stochastization plays an important role in both quenching the center of the plasma and in heat flux losses, thus lowering the amount of carbon needed to mitigate the plasma when compared to the 2D case. This study constitutes an important step forward in 'predict-first' simulations for disruption mitigation in NSTX-U and other devices, such as ITER.

Keywords: disruption mitigation, pellet injection, extended MHD, M3D-C^1, NSTX-U

(Some figures may appear in colour only in the online journal)

1. Introduction

It is well established that ITER and future tokamaks must be equipped with an effective method for injecting impurities for rapid shutdown and to mitigate the damage caused by plasma disruptions [1]. The present baseline concept for this injection system on ITER is shattered pellet injection (SPI) [2].

As an alternative to SPI, an electromagnetic pellet injection (EPI) device has been recently proposed [3, 4]. The EPI system accelerates a sabot electromagnetically with a rail gun. The sabot is a metal capsule that can be accelerated to high-velocities. At the end of its acceleration, the sabot will release the radiative payload that is composed of granules of low-Z materials, or a shell pellet containing smaller pellets. EPI would offer a fast response time and high enough speed to deposit the payloads in the plasma core in ITER. Preliminary studies have already been conducted [5] but more dedicated studies are needed.

To understand the physics involved, reliable simulations that can evaluate and predict the evolving plasma in this situation are essential. Recently, the M3D $-$ C^1 code has incorporated impurity radiation and pellet injection modules

---

[*] Author to whom any correspondence should be addressed.

1741-4326/21/116003+11$33.00

[6, 7] which allows it to perform these kinds of studies, and benchmark exercises are presently underway.

To explore the EPI concept and its potential benefits, we have conducted a series of simulations modeling the injection of a single carbon pellet in NSTX-U. To do this, a carbon ablation model [8] was incorporated in $M3D-C^1$. As a first step, the ablation model was tested by performing a simulation of carbon injection into an ASDEX-U discharge for which data exists [8]. Next, we performed a convergence study for NSTX-U covering different modeling parameters. We compare these cases and show the sensitivity to the induced thermal quench and other relevant parameters on the physical input and modeling parameters.

Although the baseline disruption mitigation system for ITER uses neon, the use of lower-Z material offers the advantage of maintaining a modest core electron temperature following the thermal quench phase. This may be important for avoiding the formation of runaway electrons. Theoretical work of Konovalov *et al* [9] suggests that as little as 5 g of Be may be adequate for both thermal quench and runaway electron mitigation in ITER. As SPI has been adopted as the baseline disruption mitigation system for ITER, there has not been much effort devoted toward low-Z material injection studies. For studies on NSTX-U, carbon, boron, or boron nitrite are the possibilities and it is envisioned that all of these would be tested. Because of the availability of carbon injection results from ASDEX-U, the initial model has used carbon. The plan is to also incorporate boron and possibly BN ablation data into $M3D-C^1$.

This paper is organized as follows: in section 2 we briefly summarize the modeling of pellets in $M3D-C^1$ and how it is coupled to the MHD equations. We also describe the carbon model that was implemented in $M3D-C^1$. In section 3 we present a comparison of our implementation with available data from ASDEX-U. Section 4 presents the NSTX-U equilibrium configuration used in the remaining studies. Section 5 presents some preliminary 2D modeling results for subsequent comparisons. In section 6 we present C-pellet disruption mitigation simulations for proposed NSTX-U experiments and show some sensitivities to modeling and physical parameters. Finally, we summarize the results in section 7.

2. Pellet-injection modeling in $M3D-C^1$

For convenience, we summarize here the physics and modeling involved in $M3D-C^1$, focusing on disruption mitigation studies. These have been extensively described in references [6, 7]. $M3D-C^1$ is a non-linear 3D extended-MHD code that uses high-order finite elements and implicit time-stepping to advance the equations in time [10].

The ablation of the impurity pellet material and its subsequent redistribution in the plasma is a complex process involving 'local' physics on the scale of the pellet diameter and global physics on the scale of the plasma minor radius. In our approach, the local physics is described by an ablation model which gives the ablation rate $\dot{N}$ as a function of the local values of the plasma temperature and density. The physical processes involved in this are described more at the end of this section. The global physics involving free-streaming along the magnetic field, the onset of instabilities, and redistribution of the pellet material is described by the MHD equations (2)–(6) [11].

The ablated material is weighted with a prescribed spatial distribution in the region surrounding the pellet position and is included as a source in the fluid equations. Different spatial distribution functions have been incorporated in $M3D-C^1$. In this work, we have used a Gaussian-like shape distribution so that the source term for the ablated material reads

$$\sigma = \frac{\dot{N}}{(2\pi)^{3/2}\Delta_\mathrm{p}^2\Delta_\mathrm{t}} \exp\left\{-\frac{(R-R_\mathrm{p})^2+(Z-Z_\mathrm{p})^2}{2\Delta_\mathrm{p}^2} - \frac{RR_\mathrm{p}\,(1-\cos(\varphi-\varphi_\mathrm{p}))}{\Delta_\mathrm{t}^2}\right\}, \tag{1}$$

where cylindrical coordinates (R, φ, Z) are employed and the (time dependent) pellet position is given by $(R_\mathrm{p}, \varphi_\mathrm{p}, Z_\mathrm{p})$. The typical size of the ablated material cloud is specified by Δ_p (poloidal width) and Δ_t (toroidal width). Limitations on these values arise due to the mesh resolution that $M3D-C^1$ uses to solve the fluid equations in 3D.

The ablated material is initialized as neutrals and all the atomic physics (ionization, recombination, radiation, etc) is calculated with the KPRAD module that is coupled to the extended MHD equations [6, 7]. Thus, different source terms σ_s are generated for main ions and each charge state of impurities (here, each charge state is considered a different species).

These source terms and the radiated energy (RE) are coupled to the fluid equations to evolve the plasma in a self-consistent way. The implementation solves a continuity equation for each charge state of each ionized species (main ions and impurities),

$$\frac{\partial n_\mathrm{s}}{\partial t} + \nabla\cdot(n_\mathrm{s}\mathbf{v}) = \nabla\cdot D\nabla n_\mathrm{s} + \sigma_\mathrm{s}. \tag{2}$$

Here, n_s is the density of each charge state of each plasma species s, D is a density diffusion coefficient usually employed for numerical stability, σ_s is the source term calculated with the KPRAD module for each charge state. The electron density is defined to satisfy the quasi-neutrality condition.

The coupling with the momentum equation was implemented in a single-fluid velocity model, i.e. all species have the same fluid velocity $\mathbf{v}$,

$$\rho\left(\frac{\partial\mathbf{v}}{\partial t} + \mathbf{v}\cdot\nabla\mathbf{v}\right) = \mathbf{J}\times\mathbf{B} - \nabla p - \nabla\cdot\Pi - \bar{\omega}\mathbf{v}, \tag{3}$$

where

$$\rho = m_i n_i + \sum_{j=1}^{Z} m_z n_z^{(j)}$$

$$\bar{\omega} = m_i\sigma_i + \sum_{j=1}^{Z} m_z\sigma_z^{(j)}.$$

Here j represents the charge state of an impurity with nuclear charge Z. The quantity $\bar{\omega}\mathbf{v}$ appears as a consequence of momentum conservation in the single fluid approximation.

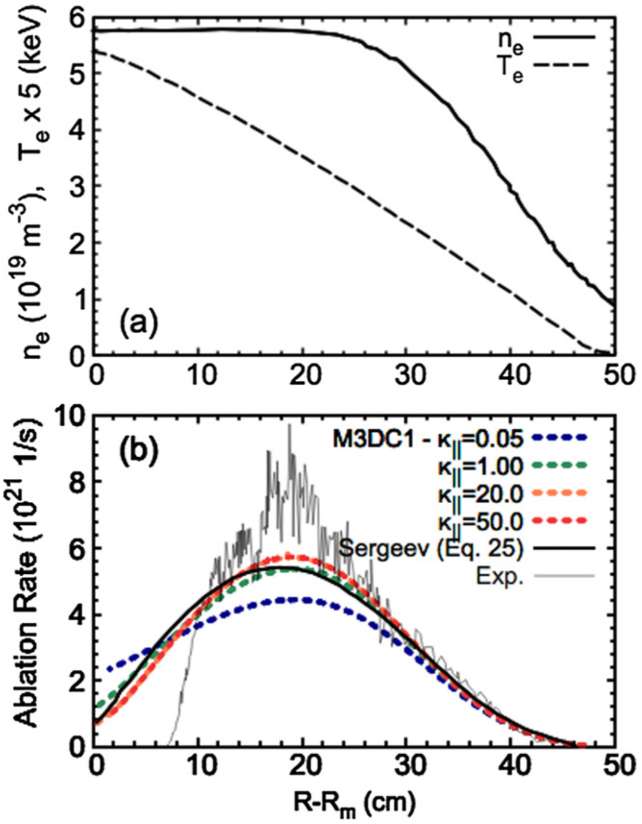

Figure 1. Comparison of the ablation rate obtained in M3D $-$ C^1 in an ASDEX-U-like plasma for which data existed. In (*a*) the plasma kinetic profiles are shown and figure (*b*) shows the ablation rate obtained with M3D $-$ C^1 for different parallel heat flux coefficients $\kappa_\parallel$, compared with results reported in reference [8]. The experimental curve, Exp., is based on the observation of the CII emission from the pellet cloud, which is assumed to be proportional to the ablation rate.

The momentum equation for electrons leads to the Ohm's law

$$\mathbf{E} = \eta\mathbf{J} - \mathbf{v} \times \mathbf{B}. \tag{4}$$

For the energy equations, there are different assumptions that were implemented, as explained in reference [7]. Here, we used the two temperature model, which evolves a temperature for the electrons:

$$n_{\rm e}\left(\frac{\partial T_{\rm e}}{\partial t} + \mathbf{v}\cdot\nabla T_{\rm e} + (\Gamma-1)T_{\rm e}\nabla\cdot\mathbf{v}\right) + T_{\rm e}(\nabla\cdot D\nabla n_{\rm e} + \sigma_{\rm e})$$
$$= (\Gamma-1)\left(\eta\mathbf{J}^2 - \nabla\cdot\mathbf{q}_{\rm e} + Q_{\rm e} + Q_\Delta - \Pi_{\rm e}:\nabla\mathbf{v}\right), \tag{5}$$

and also a temperature for all the ion species:

$$n_*\left(\frac{\partial T_{\rm i}}{\partial t} + \mathbf{v}\cdot\nabla T_{\rm i} + (\Gamma-1)T_{\rm i}\nabla\cdot\mathbf{v}\right) + T_{\rm i}(\nabla\cdot D\nabla n_* + \sigma_*)$$
$$= (\Gamma-1)\left(-\nabla\cdot\mathbf{q}_* + Q_* - Q_\Delta - \Pi_*:\nabla\mathbf{v} + \frac{1}{2}\bar{\omega}v^2\right). \tag{6}$$

Here $Q_{\rm e}$ is the electron heat source density, which is the sum of the heating or cooling from radiation and ionization, Q_Δ is the collisional transfer of energy from the ions to the electrons, and

$$\mathbf{q}_{\rm e} = -\kappa_{\rm t}\nabla T_{\rm e} - \kappa_\parallel\nabla_\parallel T_{\rm e} \tag{7}$$

is the electron heat flux. We assume the same thermal conductivities $\kappa_{\rm t}$ and $\kappa_\parallel$ for all the species. The simulations use realistic Spitzer resistivity η and effects of effective charge are properly taken into account. The quantities n_*, σ_*, Π_*, Q_* and $\mathbf{q}_*$ in the ion temperature equation are sum over all ion species of the particle densities, particle source densities, stresses, energy density sources, and heat fluxes, respectively. All the ions (main plasma ions and ionized impurities) are assumed to have the same temperature. For a detailed explanation of these equations, see reference [7].

Several ablation models have been derived for different pellet materials [8, 12, 13] in order to provide the quantity $\dot{N}$. Many of these rely on the neutral gas shielding approximation and scaling laws. For carbon pellets we implemented the model described in references [8, 14]. This model is based on the so-called shielding factor, which is the ratio of the plasma heat flux that enters into the neutral cloud and the heat flux that actually reaches the pellet surface. In reference [8], Sergeev *et al* present ablation rates for both strong and weak shielding limits and they propose a simple interpolation formula for intermediate shielding to cover both limiting cases (see equation (25) in the same reference). As a first step toward carbon ablation simulations, we have implemented this ablation model in M3D $-$ C^1. The local temperature and density needed to calculate the ablation are approximated as the average temperature weighted by the prescribed neutral cloud defined above. Recently, other ablation models have been used for carbon granule injection (and other materials) [15] and could be also implemented in M3D $-$ C^1.

3. Validating the ablation rate implementation in M3D $-$ C^1

The ablation model described in reference [8] has been used to analyze several discharges [8, 14, 16]. In order to test the implementation in M3D $-$ C^1, we have chosen one of those cases: an ASDEX–U-like plasma, which was reconstructed from the shot #3948 using the available information [8].

The pellet had an initial radius $r_{\rm p} = 0.25$ mm and was injected from the outer mid-plane region toward the plasma core. In our simulations we approximated it as a radially inward injection from the outer mid-plane. The pellet velocity was $v_{\rm p} = 485$ m s^{-1}. This initial pellet radius and velocity is the same as the experimental values and simulations reported in reference [8]. Figure 1 shows (*a*) the initial kinetic profiles and (*b*) the ablation rate, both as a function of the distance to the magnetic axis. Since the pellet is small, no significant perturbations to the plasma kinetic profiles were observed. The thin black curve in figure 1(*b*) is the experimental signal and the thicker black curve is the result reported in [8]. The four colored dashed curves are the M3D $-$ C^1 results, in which different parallel heat flux coefficients, $\kappa_\parallel$, were used. We observe that the agreement improves as the parallel heat flux increases, but that the model underpredicts the

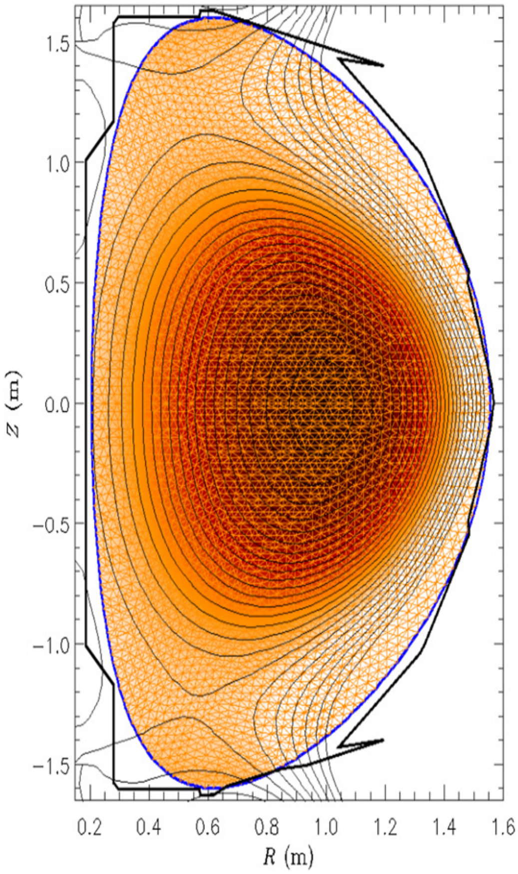

Figure 2. Computational domain, mesh and initial equilibrium configuration for the NSTX-U geometry employed. Ideal boundary conditions were used.

experiment by about 30% in the center. In these simulations we used $\kappa_\perp = 3 \times 10^{-6}$. [To obtain κ values in SI units, multiply by 1.54×10^{26} m^{-1} s^{-1} [17].]

We note here that, for very low parallel heat flux, the ablation rate becomes smaller because the heat flux is not large enough to keep the temperature surrounding the pellet high. The local temperature around the pellet becomes colder due to the radiation of the ablated material. When increasing the parallel heat flux coefficient, the ablation increases because the plasma can quickly offset the RE due to the ablated material, increasing the local temperature. At some point, increasing the parallel heat flux coefficient even more will not produce an increase in the ablation rate since the local temperature is completely balanced by the parallel heat flux and the temperature becomes uniform in a flux surface. However, as will be shown below, stochastic field lines caused by the pellet transit can change this behavior.

4. NSTX-U equilibrium

The good agreement presented in the previous section provides validation to conduct a series of a 'predict-first' simulations in which a single carbon pellet is injected into an NSTX-U-like discharge to instigate a thermal quench (the equilibrium is based on the NSTX shot #139 536 at 309 ms, and it is the same as the one used in reference [7]). We scanned over pellet injection conditions that support the EPI concept. Figure 2 shows the simulation domain, including the meshed plasma region in orange and simulation boundary contour in blue. In addition, poloidal flux equilibrium contours are shown together with the actual NSTX-U first wall in black as a reference. For these simulations we have used an ideal wall boundary condition (imposed at the blue contour in figure 2) which, as can be seen from the figure, approximates the NSTX-U wall. More realistic boundary conditions, including resistive walls and setting the ideal boundary domain further away is also possible in M3D $- C^1$ and might be included in future studies regarding pellets injection. The equilibrium has a magnetic major radius $R_\mathrm{m} = 0.99$ m, vacuum magnetic field at R_m of $B_0 = 0.44$ T, plasma current $I_\mathrm{p} = 580$ kA and $\beta = 2.25\%$. The total initial thermal energy (TE) is 69 kJ and the plasma magnetic energy (ME) is 120 kJ.

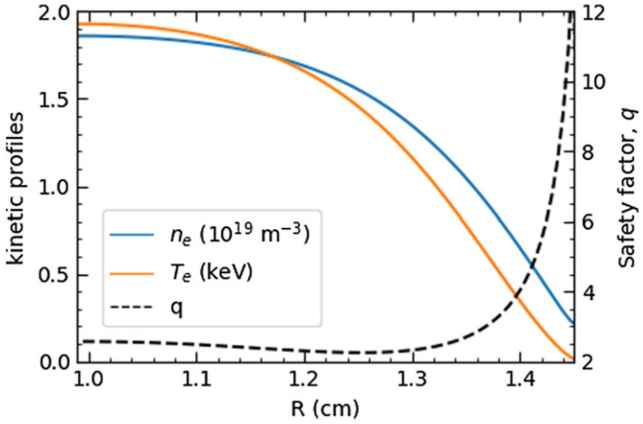

Figure 3. Initial kinetic profiles and safety factor at the midplane, as a function of the mayor radius. Magnetic axis is at $R = 0.99$ m.

Figure 3 shows the initial kinetic profiles, temperature and density, as well as the initial safety factor profile as a function of the major radius. The boundary temperature was set to 1 eV.

5. NSTX-U disruption mitigation: 2D preliminary studies

As a first step toward fully 3D carbon pellet injection simulations, we conducted a series of 2D simulations without a pellet but with an initial distribution of carbon atoms. This was performed in order to have a proxy of the amount of carbon that is needed to mitigate the plasma. The initial distribution of carbon atoms was set to be proportional to the electron density, i.e. with the same spatial distribution but scaled with a constant. Figure 4 shows the time evolution of global quantities for two cases: with an initial carbon density equals to (I) the initial electron density and (II) twice the initial electron density. The amount of carbon in case (I) is 2×10^{20} atoms while in case (II) is 4×10^{20}

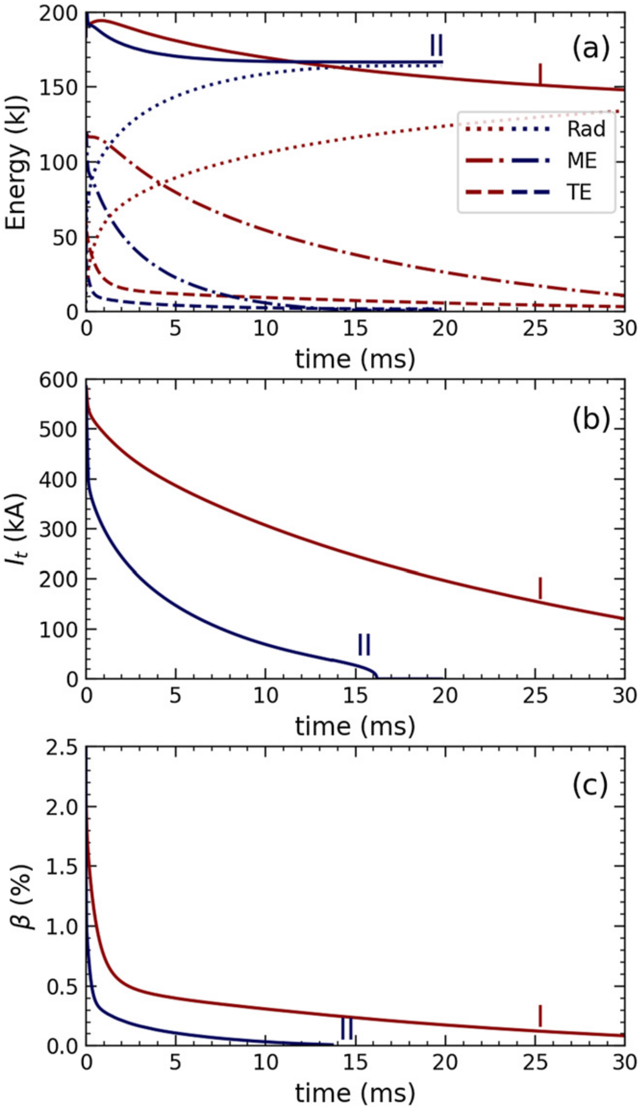

Figure 4. 2D simulations with an initial distribution of carbon that is equal to (I) the initial electron density and (II) twice the initial electron density. (*a*) Shows the TE, the ME and the radiated energy (Rad). The solid lines are the sum of the three of them. (*b*) Shows the plasma toroidal current, and (*c*) the plasma β.

atoms. As a reference, a 1 mm-radius vitreous-carbon pellet ($\rho = 1.51$ g cm^{-3}) has 3.2×10^{20} atoms, which is between these two cases.

Figure 4(*a*) shows different components of the total energy for each case: the plasma TE in dashed lines, the plasma ME in dash-dotted lines, the radiated energy (Rad) in dotted lines, and the addition of all of these components (solid lines). The drop in this solid lines represent the heat that went into the wall (heat flux). For case (II) this was only ~ 25 kJ or 13% of the total plasma energy. Figures 4(*b*) and (*c*) show the plasma current and plasma β, respectively. We observe that in both cases the plasma is quenched (particularly case (II)), suggesting that the amount of carbon in a 1 mm-radius pellet would be enough to mitigate the plasma if it were entirely ablated.

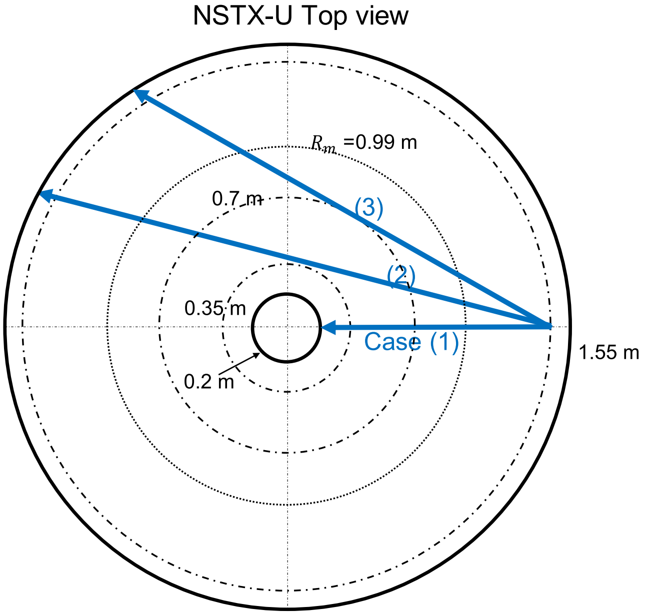

Figure 5. Schematic NSTX-U top view showing the different injection directions chosen in the simulations. Case (1)–(3) are referred in sections 6.1–6.4, respectively.

6. NSTX-U disruption mitigation via pellet injection

Based on the previous 2D simulations, we have taken this amount of carbon in a 1 mm-radius pellet (3.2×10^{20} atoms) as a reference case in this study. In this section we present several cases of carbon pellet injection scanning over different parameters. The injection was from the outer mid-plane. Figure 5 shows a schematic top-view of the device. Blue arrows represent the injection directions considered in this work. Case (1) will be discussed in sections 6.1 and 6.2, while case (2) will be discussed in section 6.3. Case (3) is a shell pellet which will be discussed in section 6.4

Regarding the ablated material cloud size (see equation (1)), we have chosen $\Delta_t = 50$ cm and $\Delta_p = 5$ cm. Even though it is not shown here, reducing the ablated cloud even more does not lead to a significant change in global quantities but requires much smaller time steps and increased spatial resolution making the simulations much more expensive. The density diffusion term in the continuity equation for each species ranged between 30–150 m^2 s^{-1} to avoid numerical instabilities. The plasma viscosity was taken to be 2.58×10^{-6} kg m^{-1} s^{-1}. These quantities can be reduced using a finer mesh but that would require much more computational resources, being unpractical for convergence studies. Further studies targeted to a particular configuration might have smaller values in these modeling parameters.

6.1. Case 1: scan over pellet velocity

Figure 6 shows different global quantities as a function of the pellet position for three different velocities: 1000, 500 and 300 m s^{-1}. In all these cases, $\kappa_\parallel$ was set to 1. As a reference, the outer wall is at approximately $R = 1.55$ m while the inner wall

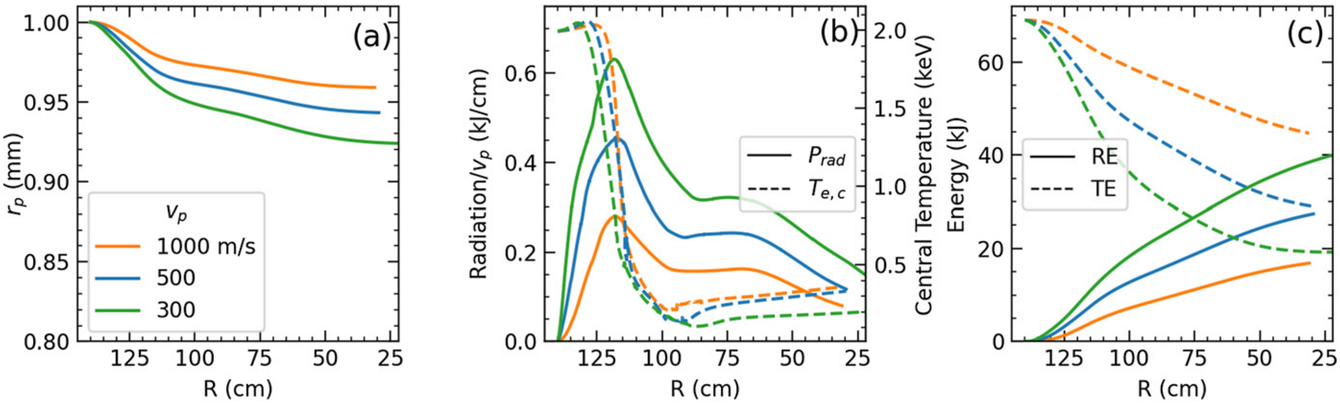

Figure 6. Pellet injection along the trajectory indicated as 'case (1)' in figure 5. Here, the figure shows a scan over three pellet velocities: 1000, 500 and 300 m s^{-1}, as a function of the pellet position. (*a*) Shows the pellet radius, (*b*) the radiated total power normalized by the pellet velocity (solid lines) and plasma central electron temperature (dashed lines), and (*c*) the RE and plasma TE. For all these cases $\kappa_\|$ was set to 1.

is at $R = 0.2$ m. The initial pellet position was set to $R = 1.4$ m which is just in the inner side of the separatrix. Figure 6(*a*) shows the pellet radius. Figure 6(*b*) shows the radiated power normalized by the pellet velocity (solid lines) and the plasma electron central temperature (dashed lines). Figure 6(*c*) shows the TE and RE.

As can be seen from the pellet radius, all the three cases have shown a partial or incomplete pellet ablation: only 11% of the pellet material was ablated for $v_\mathrm{p} = 1000$ m s^{-1} and only 21% for 300 m s^{-1}. The first thing to note is that 1000 m s^{-1} is a high velocity for a small size device such as NSTX-U, therefore reducing the velocity from 1000 m s^{-1} to 300 increased the ablation substantially. This also increases the radiation and produced a more significant drop in the plasma TE. However, when looking at the plasma central temperature, it can be observed that it falls more abruptly than the TE but, after it reaches a minimum, it increases slowly in time as the pellet finishes its path through the plasma.

To better understand this, we show in figure 7 four time slices of the plasma electron temperature together with the corresponding Poincare plot, for the case in which $v_\mathrm{p} = 1000$ m s^{-1}. Figure 7(*a*) shows the central temperature as a function of time, with different labels (I)–(IV) corresponding to 0.052, 0.235, 0.438, 1.09 ms. The corresponding 'heat-maps' of the temperature (at the poloidal plane $\varphi = 0$ that contains the injection path) and Poincare plots at those times are shown in figure 7(*b*). Pellet position is also indicated in the Poincare plots with a circle.

The plasma response and the thermal collapse due to the pellet ablated material is clearly seen in the temperature heat-maps. At panel (I), the pellet is starting to travel inside the plasma separatrix and produces field line stochastization in the outer region while the core remains unperturbed. At (II), the pellet has propagated to the $q = 2.4$ surface ($r/a = 0.38$). The core electron temperature has dropped from about 2000 eV to about 1000 eV. At this point the plasma central temperature is falling very sharply. The Poincare plot shows that the core flux surfaces are broadening and becoming partially stochastic. The field lines at the pellet position are now linked to the plasma core but not to the edge. Therefore, the heat flux that balances the pellet radiation is coming primarily from the core and, hence, the plasma temperature becomes hollow. At (III), the pellet has reached the magnetic axis. The electron temperature around the magnetic axis has dropped to about 200 eV, but the region surrounding the magnetic axis is at a higher electron temperature of over 500 eV. At this point the stochastization spreads to the edge and therefore the temperature at the center starts rising due to the hotter edge plasma. Finally, in the last time slice, panel (IV), corresponding to $t = 1.09$ ms, the pellet is almost exiting the plasma from the inboard side. The resulting plasma is starting to reform core flux surfaces but with a flattened electron temperature above 250 eV.

These sequences of images show that a 2 mm diameter carbon pellet traveling at 1 km s^{-1} through an NSTX plasma with a core electron T_e of ~ 2 keV does not fully ablate and a full thermal quench is not attained from the injection of a single pellet of this size. This is also observed in figure 6(*c*) where the TE does not drop substantially to quench the plasma.

6.2. Case 1: scan over parallel thermal conductivity

In the previous case the parallel thermal conductivity, $\kappa_\|$, was set to 1 (internal units). However, the results from figure 1 suggest that a higher $\kappa_\|$ would increase the ablation rate, since the parallel heat flux will be larger. Figure 8 shows a scan for $\kappa_\| = 50, 1$, and 0.02. In this case we fixed the pellet velocity to 300 m s^{-1}.

With very low parallel heat flux $\kappa_\| = 0.02$, the temperature surrounding the pellet falls due to the radiation which in turns lowers the ablation rate. Increasing the parallel thermal conductivity to $\kappa_\| = 1.0$ makes the temperature surrounding pellet higher, enhancing the ablation and radiation. However, when increasing $\kappa_\|$ even more, to $\kappa_\| = 50$, we observe that the ablation and radiation are reduced.

These trends can be explained by looking at the Poincare plots which are similar to that shown in figure 7(*b*) for $v_\mathrm{p} = 1000$ m s^{-1}. Before the pellet reaches the core, the stochastization links the pellet position with the plasma boundary

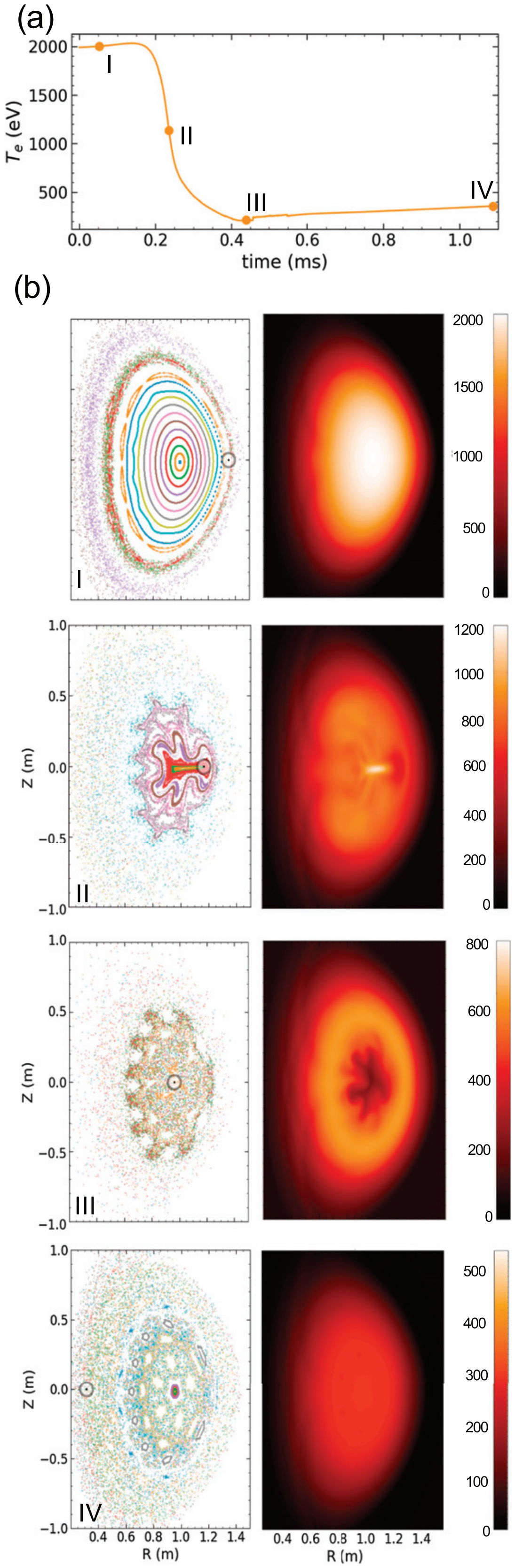

Figure 7. (*a*) Central plasma electron temperature as a function of time and (*b*) plasma electron temperature 'heat map' and Poincare plots for different times as marked in (*a*). Pellet velocity is 1000 m s^{-1} and was injected along the path indicated as 'case (1)' in figure 5.

which cools the plasma temperature faster than previous cases. Once the pellet is at the core region, the stochastization at the pellet position no longer reaches the boundary producing an enhancement in the radiation and in the ablation. However, when the pellet continues through the inner part of the plasma, the stochastization is complete and again links the pellet position with the boundary, cooling the plasma. Even though the RE is smaller than in the other two cases, the TE drops to a lower value. This is because a larger fraction is lost through the wall.

Contrary to the AUG-like case presented in figure 1, increasing $\kappa_\parallel$ does not necessarily increase the ablation, as it is constrained by the stochastization that the pellet might produce.

6.3. *Case 2: injection with a toroidal velocity*

In all the previous cases, the pellet was injected radially inward, which corresponds to case (1) in figure 5. To increase the pellet ablation fraction, a larger radius pellet which also has a toroidal velocity component was simulated, which is labeled as case (2) in figure 5. Even though M3D $-$ C^1 has the capability to model the injection of several small pellets, such as would be the case with SPI, the use of a larger diameter pellet is an approximation to an array of smaller pellets since the purpose is to increase the effective surface area and therefore the ablation. In this case, we employed a 3.6 mm radius pellet. The pellet is hollow and the thickness was adjusted so that the amount of material is the same as in the previous cases. In this way, the surface is increased by $\sim$ 13 and would be roughly similar to having an array of smaller pellets with the same total surface and material. This case is shown in figure 9 for a pellet velocity of 1000 m s^{-1} and $\kappa_\parallel = 1.0$.

Figure 9(*a*) shows the radiation power and the plasma central electron temperature during the time the pellet is passing through the plasma. At $t \approx 0.45$ ms the pellet reaches the magnetic axis for the first time, showing a minimum in the radiated power as explained with the previous case. At $t \approx 1.4$ ms the pellet reaches the minimum major radius position of 0.35 m. Here again the radiated power presents a local minimum value since the pellet is in the inner side of the plasma. The pellet reenters the plasma from the inner side and reaches again the magnetic axis at $t \approx 2.3$ ms and, finally, at $t \sim 2.9$ ms the pellet hits the outer wall. The total ablated material was $\sim 32\%$, showing a significant increase from the radial injection of the smaller pellet, which was around $\sim 11\%$.

Figure 9(*b*) shows the plasma current (solid line) the plasma thermal (dotted line), magnetic (dashed line) and radiated (dash-dotted line) energy as a function of time for the entire simulation, which ran up to 23 ms. We can observe that the amount of ablated material $\sim 1 \times 10^{20}$ atoms starts to produce a current quench (CQ), somewhat consistent with the 2D estimation. The CQ seems to be stronger than case I in figure 4. This is because, in 3D simulations the stochastization of the field lines enhances the heat flux loses through the wall, as explained in section 6.2. In this case, it can be inferred to be

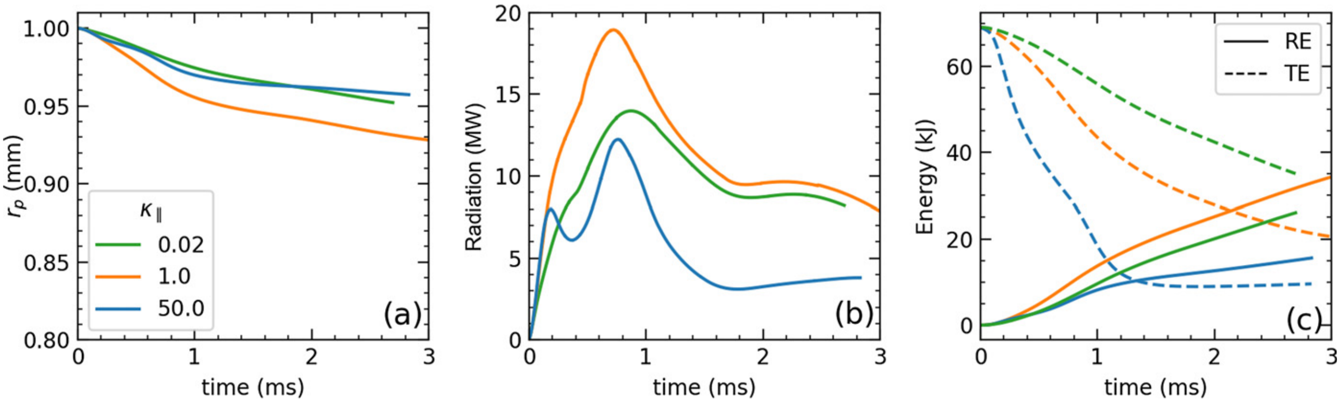

Figure 8. Pellet injection along the trajectory indicated as 'case (1)' in figure 5. Here, the figure shows a scan over different parallel thermal conductivities, $\kappa_\parallel$, for a pellet velocity of $v_\mathrm{p} = 300$ m s^{-1}. (*a*) Pellet radius, (*b*) radiation power and (*c*) RE (solid) and TE (dashed).

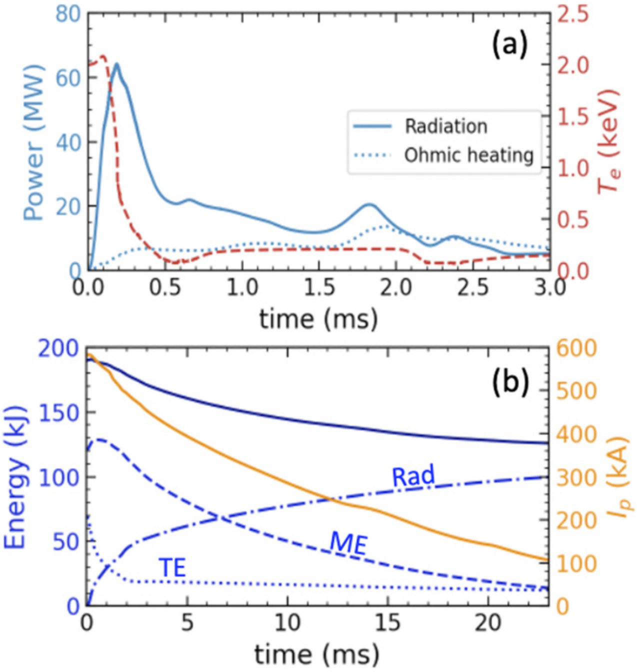

Figure 9. (*a*) The total radiated power and the central electron temperature for the case of a tangential hollow pellet injection at 1 km s^{-1}, along the trajectory shown as 'case (2)' in figure 5. (*b*) Time evolution of the plasma thermal energy, TE (dotted), plasma magnetic energy, ME (dashed), and radiated energy, Rad (dash-dotted). The blue solid line is the sum of these three contributions. The plasma current is also shown in orange (solid). $\kappa_\parallel$ was set to 1.

~ 60 kJ at $t = 23$ ms (approximately 30% of the entire initial plasma TE and ME).

6.4. Case 3: shell pellet

The fact that in all previous simulations the ablation was incomplete, even at velocities of ~ 300 m s^{-1} suggests that high velocity pellets may have the potential for penetration into the plasma core in larger machines, for example in ITER. This is the basic idea of a shell pellet, which protects the payload until it reaches the core and deposits its payload there in order to induce an inside–out thermal quench. Experiments [18] at DIII-D have demonstrated this technique and simulations were also conducted [19] using the NIMROD code [20].

As a test case to this approach, we performed a simulation which tries to resemble the injection of a hollow carbon pellet filled inside with carbon dust. The pellet was injected along the trajectory indicated with case '3' in figure 5, with a velocity of 1000 m s^{-1}. In this case, the pellet is first ablated as usual, following the ablation formula described in section 2, but once it reached the $R \approx 1.1$ m position ($\sqrt{\psi_\mathrm{n}} \approx 0.2$) at $t \sim 0.41$ ms, we turned off the ablation, which gave values around $\dot{N} \sim 10^{23}$ atoms/s, and switched the deposition rate to a constant (larger) value of $\dot{N} = 1.14 \times 10^{24}$ atoms/s. This constant deposition rate was continued to be centered at the (virtual) pellet position and distributed with the same Gaussian shape presented in section 2, but the toroidal cloud size was increased from $\Delta_\mathrm{t} = 0.5$ to 1. This rate was maintained for 0.2755 ms. The total amount of carbon deposited (including the initial ablation) was 3.8×10^{20} atoms, which is similar to the case (II) that was presented as a proxy in section 5. After that time the deposition was turned off. The main reason for increasing Δ_t is to avoid numerical instabilities that may arise when spreading a large amount of ablated material in a small volume.

The ablation rates of about 10^{23} atoms/s and 10^{24} atoms/s is what a 1 mm radius pellet and a 3.6 mm radius pellet would be subjected to. The goal is to ensure that the ablated shell material does not trigger a thermal quench before it reaches the desired depth. The objective of the studies presented here was to see how the plasma would respond if an ideal shell pellet were used. At an ablation rate of 10^{23} atoms/s, approximately 13% for the shell material would be ablated; this is insufficient material to trigger a thermal quench. The higher ablation rate after the shell reached $R = 1.1$ m was to force deposition of the full payload mass before the radiative payload left the $R = 1.1$ m surface from the inboard side. These are simplifications aimed at comparing the plasma response for full radiative payload deposition inside the $R = 1.1$ m surface versus those from cases (1) and (2). In regard to the shell design, the shell needs to withstand the

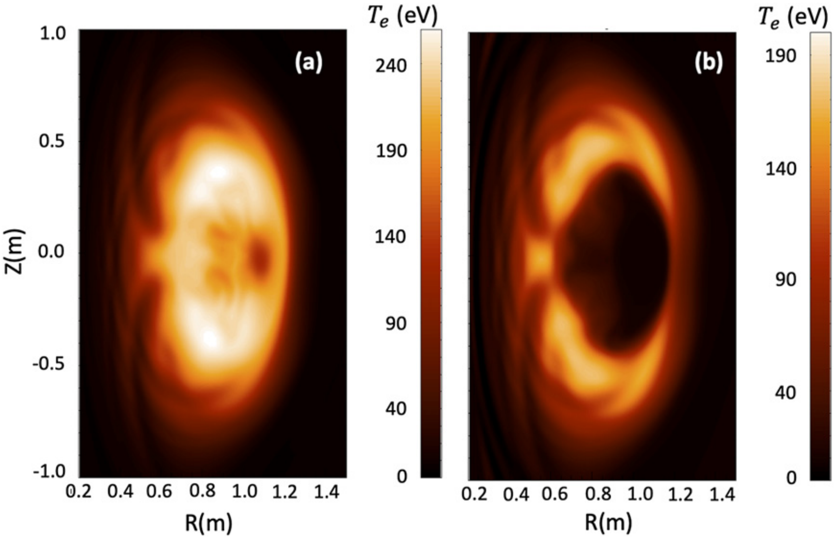

Figure 10. Plasma electron temperature 'heat-maps' for the shell-pellet approximation injected along the trajectory indicated as 'case (3)' in figure 5. (*a*) Shows the temperature just before turning on the large constant deposition rate, at $t = 0.41$ ms, and (*b*) after 0.05 ms of turning it on ($t = 0.46$ ms).

acceleration forces and be resistant to too much ablation, something that needs more consideration, both through experiments and modeling.

Figure 10 shows the electron temperature (*a*) just before turning on the large deposition rate, at $t = 0.41$ ms, and (*b*) shortly after turning it on ($t = 0.46$ ms).

The darker region around $R \sim 1.1$ m and $Z \sim 0$ that is observed in figure 10(*a*) corresponds to the pellet position and ablated cloud material that cools the surrounding plasma. It is clearly observed that after turning the large constant deposition rate on, the plasma central temperature collapses and the plasma temperature becomes hollow.

Figure 11(*a*) shows, as with the previous case, the radiated power and ohmic heating (in blue) as a function of time as well as the central temperature (in red). Figure 11(*b*) shows the plasma TE, ME and radiated energy (Rad). The blue solid line represents the sum of the three terms. The toroidal plasma current is also shown for reference in orange. We observe that, as in previous cases, the central temperature falls down to a couple of hundreds of eVs during the ablation phase, before the pellet reaches the core. When turning on the large constant deposition rate at $t \sim 0.41$ ms, the central temperature collapses while the surrounding temperature remains higher and decays slower.

Even though the amount of carbon is similar to the 2D case shown in section 5, here the plasma quench occurs much faster than in the case II of figure 4. One main difference here is the stochastization of the field lines, not present in 2D simulations, that enhance the heat flux toward the wall. This can be noted as the drop in the blue solid line in figure 11(*b*). In the 2D case, the heat that went to the wall was almost $\sim 13\%$ of the total plasma energy, as shown in figure 4(*a*), but here the total heat that reached the wall was approximately 60 kJ ($\sim 31\%$ of the total plasma energy content). The stochastization of the field lines, that in this case cover the entire cross section, should also prevent the formation of runaway electrons, but this analysis was not in the scope of the present paper.

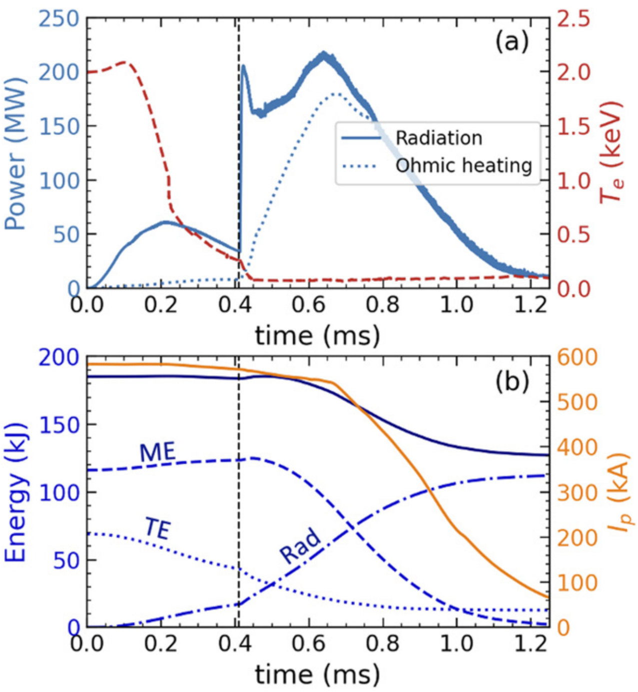

Figure 11. (*a*) The total radiated and ohmic heating power (blue), and the central electron temperature (red) for a shell pellet injection at 1 km s^{-1}, following the trajectory indicated as case (3) in figure 5. (*b*) Plasma thermal energy, TE, (dotted), plasma magnetic energy, ME, (dashed) and total radiated energy, Rad, (dash-dotted) are shown in blue. The solid blue line is the sum of all of them. The drop indicates the heat flux flowing into the wall. Also shown is the plasma toroidal current in an orange solid line. The vertical black line indicates the time at which the shell pellet payload is released.

7. Summary

We have conducted a broad range of simulations modeling single C-pellet injections in an NSTX-U-like plasma in support of the EPI concept. This set of simulations constitute an important step toward predict-first simulations for disruption mitigation in NSTX-U and other devices, such us ITER. We have incorporated a carbon ablation model in $\mathrm{M3D}-C^1$ and tested it in an ASDEX-U-like discharge for which data exists, obtaining very good agreement. Preliminary 2D simulations in NSTX-U suggested that the carbon content in 1 mm radius vitreous carbon pellet ($\sim 3.2 \times 10^{20}$ atoms) should be enough to mitigate the plasma if entirely ablated and have used this as a proxy for the amount of carbon that was considered for 3D pellet injection simulations.

We performed a wide range of 3D simulations, injecting a single C-pellet from the outer midplane, scanning over different modeling parameters such as parallel thermal conductivity and pellet velocity, among others, to show the sensitivity of the induced thermal quench and other relevant quantities. When injecting a 1 mm-radius pellet radially inward, the simulations show that the pellet is partially ablated, from 11%, for $v_\mathrm{p} = 1000\ \mathrm{m\ s^{-1}}$, to 21%, for $300\ \mathrm{m\ s^{-1}}$, leading to post-TQ temperature of hundreds of eVs which is not enough to produce a rapid CQ. We also injected the pellet with an initial toroidal velocity to maximize the path length and with increased pellet radius in order to increase the effective ablation surface. This would be similar to injecting an array of smaller pellets. In this case, in which the pellet velocity was $1000\ \mathrm{m\ s^{-1}}$, the ablation increased to $\sim 32\%$ of the amount in 1 mm-pellet. Even though it was still an incomplete ablation relative to this amount, it was enough to produce a CQ with a timescale of $\sim$ 15–20 ms, but in which the stochastization of the field lines also played an important role leading to about 30% of the total energy flowing into the wall.

We also have explored the injection of a shell pellet filled with carbon dust. We have modeled the carbon dust deposition by switching the ablation rate formula to a larger constant deposition rate for a short period of time. The total amount of carbon deposited was 3.8×10^{20} atoms. In this simulation the pellet produced a core temperature collapse followed by a fast thermal and CQ.

The broad set of scans in this work did not allow the use of very fine mesh grids and a lower density diffusion coefficient. However, future work will be focused on a particular pellet configuration and a particular discharge that includes a $q = 2$ surface. This will allow us to refine numerical modeling parameters that may affect higher toroidal modes numbers.

Finally, the shell pellet concept offers the promise of an inside to outside thermal quench, as one need not rely on plasma MHD to transport the radiative material to the core. However, exploration of this concept is at an early phase. Testing the capability of this concept would be a high-priority activity on NSTX-U and may be the best concept for thermal energy load mitigation. At this point, reliable MHD modeling (benchmarked with present experiments) is the only way to project to ITER. To develop this capability, injection of well-defined radiative payload (single as well as multiple spherical pellets of known size, velocity, and composition—which would be possible using EPI) would also be necessary to develop the needed modeling capability.

Acknowledgments

This work was supported by the U.S. Department of Energy under DOE Contract DE-AC02-09CH11466 and the SciDAC CTTS. This research used resources of the National Energy Research Scientific Computing (NERSC) Center, a DOE Office of Science User Facility supported by the Office of Science of the U.S. Department of Energy under Contract No. DE-AC02-05CH11231. CFC also acknowledges the support by the US DOE under Contract DE-SC0021385.

ORCID iDs

C.F. Clauser https://orcid.org/0000-0002-2597-5061
S.C. Jardin https://orcid.org/0000-0001-6390-6908
R. Raman https://orcid.org/0000-0002-2027-3271
B.C. Lyons https://orcid.org/0000-0003-3232-1581
N.M. Ferraro https://orcid.org/0000-0002-6348-7827

References

[1] Hender T.C. *et al* 2007 Chapter 3: MHD stability, operational limits and disruptions *Nucl. Fusion* **47** 128S–202

[2] Commaux N. *et al* 2016 First demonstration of rapid shutdown using neon shattered pellet injection for thermal quench mitigation on DIII-D *Nucl. Fusion* **56** 046007

[3] Raman R., Lay W.-S., Jarboe T.R., Menard J.E. and Ono M. 2019 Electromagnetic particle injector for fast time response disruption mitigation in tokamaks *Nucl. Fusion* **59** 016021

[4] Raman R., Lunsford R., Clauser C., Jardin S.C., Menard J.E. and Ono M. 2021 Prototype tests of the electromagnetic particle injector-2 for fast time response disruption mitigation in tokamaks *Nucl. Fusion* (submitted)

[5] Lunsford R., Raman R., Brooks A., Ellis R.A. and Lay W.-S. 2019 Modeling of ablatant deposition from electromagnetically driven radiative pellets for disruption mitigation studies *Fusion Sci. Technol.* **75** 767–74

[6] Lyons B.C., Kim C.C., Liu Y.Q., Ferraro N.M., Jardin S.C., McClenaghan J., Parks P.B. and Lao L.L. 2019 Axisymmetric benchmarks of impurity dynamics in extended-magnetohydrodynamic simulations *Plasma Phys. Control. Fusion* **61** 064001

[7] Ferraro N.M., Lyons B.C., Kim C.C., Liu Y.Q. and Jardin S.C. 2019 3D two-temperature magnetohydrodynamic modeling of fast thermal quenches due to injected impurities in tokamaks *Nucl. Fusion* **59** 016001

[8] Sergeev V.Y., Bakhareva O.A., Kuteev B.V. and Tendler M. 2006 Studies of the impurity pellet ablation in the high-temperature plasma of magnetic confinement devices *Plasma Phys. Rep.* **32** 363–77

[9] Konovalov S., Leonov V., Khayrutdinov R., Lukash V., Medvedev S., Putvinski S., Zhogolev V., Aleynikov P. and Kavin A. 2012 Studying the capabilities of Be pellet injection to mitigate ITER disruptions (*24th IAEA Fusion*

Energy Conference 8-13 October) (http://www-naweb.iaea.org/napc/physics/FEC/FEC2012/papers/338_ITRP138.pdf) (San Diego, California, United States)

[10] Jardin S.C., Ferraro N., Breslau J. and Chen J. 2012 Multiple timescale calculations of sawteeth and other global macroscopic dynamics of tokamak plasmas *Comput. Sci. Discovery* **5** 014002

[11] Samtaney R., Jardin S.C., Colella P. and Martin D.F. 2004 3D adaptive mesh refinement simulations of pellet injection in tokamaks *Comput. Phys. Commun.* **164** 220–8

[12] Parks P.B., Turnbull R.J. and Foster C.A. 1977 A model for the ablation rate of a solid hydrogen pellet in a plasma *Nucl. Fusion* **17** 539–56

[13] Parks P.B. and Turnbull R.J. 1978 Effect of transonic flow in the ablation cloud on the lifetime of a solid hydrogen pellet in a plasma *Phys. Fluids* **21** 1735–41

[14] Kuteev B.V., Sergeev V.Y. and Tsendin L.D. 1984 Interaction of carbon pellets with a hot plasma *Sov. J. Plasma Phys.* **10** 675

[15] Lunsford R., Bortolon A., Maingi R., Mansfield D.K., Nagy A., Jackson G.L. and Osborne T. 2019 Supplemental ELM control in ITER through beryllium granule injection *Nucl. Mater. Energy* **19** 34–41

[16] Sergeev V.Y., Egorov S.M., Kuteev B.V. and Miroshnikov I.V. 1994 Plasma diagnostics on ASDEX upgrade by means of carbon pellet injection (*ECA: 21st EPS Conference on Controlled Fusion and Plasma Physics* June 27 - July 1) (Montpellier, France vol 18B Part III) (http://libero.ipp.mpg.de/libero/PDF/EPS_21_Vol3_1994.pdf)

[17] As a reference, for a $T = 1$ keV, $n = 1 \times 10^{19}$ m^{-3} deuterium plasma the Spitzer–Härm electron and ion parallel thermal conductivities are $\kappa_{\|,}$e $\approx$ 4.1 $\times$ 10^{29} m^{-1} s^{-1} and $\kappa_{\|,}$i $\approx$ 8.2 $\times$ 10^{27} m^{-1} s^{-1}, respectively.

[18] Hollmann E.M., Parks P.B., Shiraki D., Alexander N., Eidietis N.W., Lasnier C.J. and Moyer R.A. 2019 Demonstration of tokamak discharge shutdown with shell pellet payload impurity dispersal *Phys. Rev. Lett.* **122** 065001

[19] Izzo V.A. and Parks P.B. 2017 Modeling of rapid shutdown in the DIII-D tokamak by core deposition of high-z material *Phys. Plasmas* **24** 060705

[20] Sovinec C.R. *et al* 2004 Nonlinear magnetohydrodynamics simulation using high-order finite elements *J. Comput. Phys.* **195** 355–86